Maximizing the Accessibility in DNA Origami Nanoantenna Plasmonic Hotspots

Cindy Close, Kateryna Trofymchuk, Lennart Grabenhorst, Birka Lalkens, Viktorija Glembockyte, and Philip Tinnefeld*

DNA nanotechnology has conquered the challenge of positioning quantum emitters in the hotspot of optical antenna structures for fluorescence enhancement. Therefore, DNA origami serves as the scaffold to arrange nanoparticles and emitters, such as fluorescent dyes. For the next challenge of optimizing the applicability of plasmonic hotspots for molecular assays, a Trident DNA origami structure that increases the accessibility of the hotspot is introduced, thereby improving the kinetics of target molecule binding. This Trident NanoAntenna with Cleared HOtSpot (NACHOS) is compared with previous DNA origami nanoantennas and improved hotspot accessibility is demonstrated without compromising fluorescence enhancement. The approach taps into the potential of Trident NACHOS for single-molecule-based plasmonic biosensing.

1. Introduction

The DNA origami technique enables targeted placement of nanoobjects in defined patterns.[1–13] This unique way of engineering with the help of nucleic acids at dimensions below the wavelength of electromagnetic radiation proved to be especially advantageous for the field of nanophotonics.[14–17] Firm positioning of a plasmonic nanoparticle (NP), thereby controlling the distance of its surface to a molecule, is, for example, one of the main parameters to control the interaction of a target molecule with the excited localized surface plasmon resonance (LSPR), as used in surface-enhanced spectroscopies such as

Raman or fluorescence.[15,18–28] The LSPR effect is based on the interaction of electromagnetic radiation with conduction electrons of noble metal NPs and the resonance strongly depends on the correspondence of the excitation wavelength to size, shape, and material of the NP.[29,30] When placing a single fluorescent molecule in proximity, multiple effects simultaneously influence transitions between electronic states. The increased intensity of the local electric field, created by LSPR, and distance to NPs affect excitation rates, as well as radiative and non-radiative decay rates.[18,31,32] In consequence, the distance dependence results in a continuous transition from fluorescence quenching (FQ) in close proximity and fluorescence enhancement (FE) at an increased distance, reaching maximum FE values at a defined position (hotspot).[21,33,34] Besides their distance, the size of NPs influences the relation of quenching and enhancement. In first approximation, larger particles lead to higher FE.[35,36] Finally, electric field enhancement only occurs at the poles of particles or in between particles depending on the relative alignment of particles, emitters, and the excitation polarization.

The first examples of so-called dimer nanoantennas (NAs) were achieved using electron-beam lithography, relying on dyes stochastically placed in the hotspot.[33] Controlled positioning of a fluorophore in the hotspot of two NPs was presented by Acuna et al., utilizing a pillar-shaped DNA origami that bears anchoring poly-adenine strands for the attachment of two gold (Au) NPs (functionalized via thiol chemistry with poly-thymine) at a fixed position, while placing a fluorophore in between (**Figure 1**a).[37,38] FE values up to 117-fold were achieved by positioning an ATTO647N molecule in the created 23 nm gap between two 100 nm Au NPs.[35,36] Although FE values of over 400-fold were reached in refined DNA origami structures, the mentioned NA designs suffered from the limitation that the hotspot region was blocked by the DNA origami itself, thereby prohibiting the placement of a detection assay in this region.[29,39–41] To this end, the DNA origami NA proved to be applicable for the detection of Zika virus-specific oligonucleotides, both in buffer and heat-deactivated serum.[39] However, due to the steric hindrance in the hotspot, only the binding of one plasmonic NP was feasible, resulting in moderate FE values (approximately sevenfold) in the monomer NA arrangement.

Only recently, a DNA origami dimer NanoAntenna with Cleared HOtSpot (NACHOS, Figure 1b) was realized that

C. Close, K. Trofymchuk, L. Grabenhorst, V. Glembockyte, P. Tinnefeld
Department of Chemistry and Center for NanoScience
Ludwig-Maximilians-Universität München
Butenandtstr. 5-13, 81377 Munich, Germany
E-mail: philip.tinnefeld@cup.uni-muenchen.de
B. Lalkens
Institut für Halbleitertechnik
Laboratory for Emerging Nanometrology LENA
TU Braunschweig
Langer Kamp 6a/b, 38106 Braunschweig, Germany

The ORCID identification number(s) for the author(s) of this article can be found under https://doi.org/10.1002/admi.202200255.

**ADVANCED
SCIENCE NEWS**
www.advancedsciencenews.com

**ADVANCED
MATERIALS
INTERFACES**
www.advmatinterfaces.de
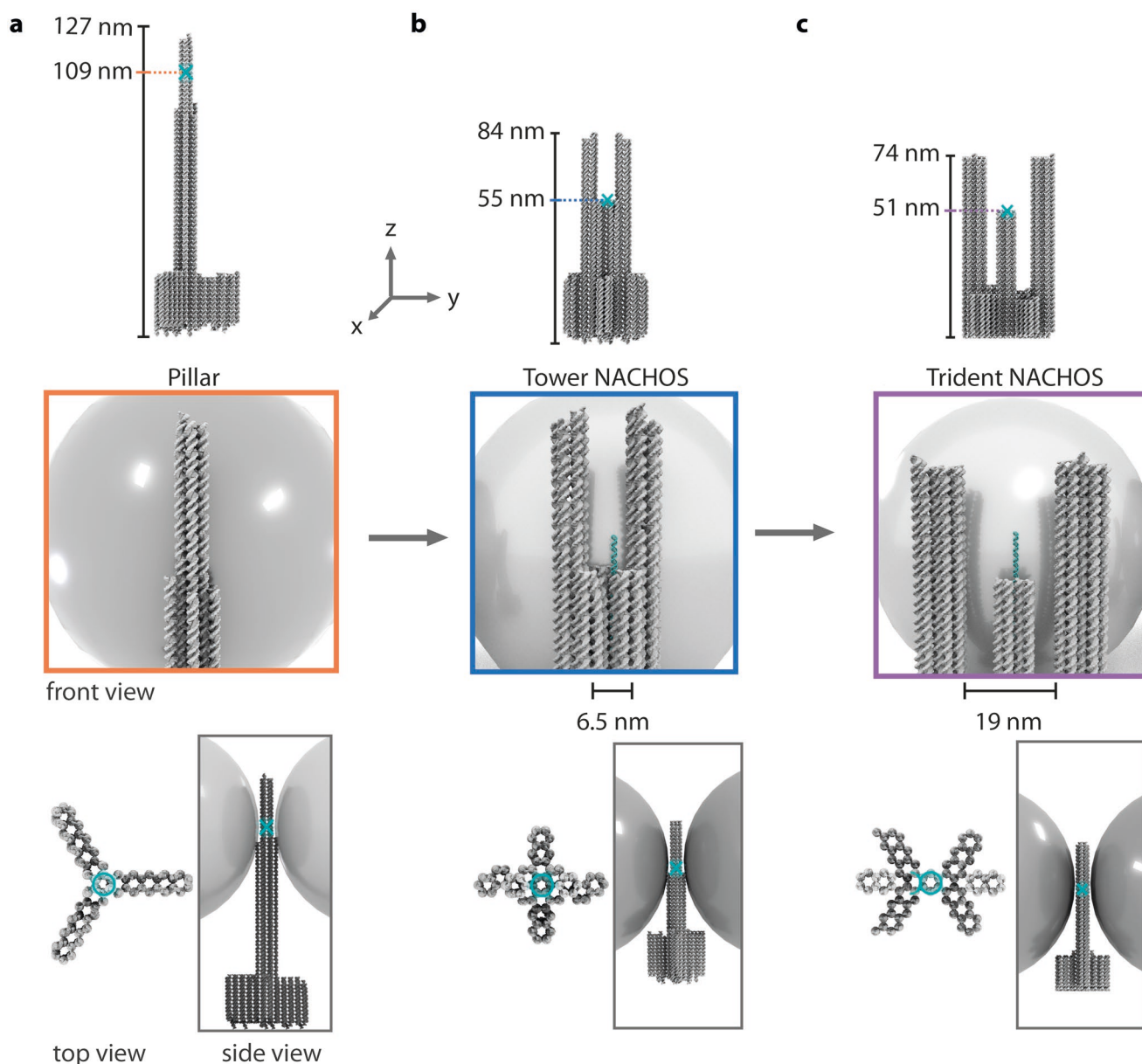
Figure 1. Schematic representation of three different DNA origami designs used for DNA origami NAs: a) Pillar,[29,39] b) Tower NACHOS,[42,43] c) Trident NACHOS. Hotspot position (marked with a cross) and overall height (top); Zoom-in on the hotspot regions showing the attached NP (100 nm diameter) and comparing the regions that are cleared from DNA origami and can be utilized for placing diagnostic assays (middle); Top view of DNA origami and side view with 100 nm NPs. Hotspot region is marked in cyan (bottom).

provides space of ≈12 nm × 6.5 nm in the plasmonic hotspot region between the particles, freed from DNA, for placing a biomolecular assay, while maintaining maximum FE values of over 400-fold.[42] The achieved high signal amplification enabled the first detection of 34 nt ssDNA and even single antibodies using a portable smartphone microscope.[35,42–44]

The experience with developing DNA origami NAs has yielded a few design rules for further evolution. One lesson learned is that FE distributions are commonly quite broad, reflecting that a small deviation from the exact placement of the structural components can have detrimental impact on the properties of the individual constructs. Heterogeneity is likely related to non-spherical NPs that bind in varying orientations,

the distribution of positions of the bound strands on NPs, as well as a flexible dye position and orientation in the DNA origami. While the dye itself should be rotating freely, it was shown that fluorophores often stick to regions inside the DNA origami.[45] Nevertheless, FE distributions are well reproducible within each DNA origami design, and the respective average FE correlates well with the maximally achieved FE values. The sensitivity of FE on subtle factors, however, indicates that the structural control of the immediate hotspot surrounding is critical. We concluded that rigid and distance-controlled arrangement of NPs is obligatory, implying that NP binding should occur as close to the hotspot as possible, while not compromising the space required for assays in the hotspot. Binding NPs on a

**ADVANCED
SCIENCE NEWS**
www.advancedsciencenews.com

**ADVANCED
MATERIALS
INTERFACES**
www.advmatinterfaces.de

flat DNA origami without a steric blockade resulted in heterogeneity (due to, e.g., NP size distribution), which limited the achievable FE, but could still be useful, for example, for Raman studies.[46–49]

In NACHOS, this paradigm was followed by placing two rigid pillars next to the hotspot, thereby creating a space that was similar to the size of the central pillar in the first generation of DNA origami NAs. In order to tap the full potential of DNA origami NAs for fluorescence-enhanced single-molecule biosensing, here, we followed the line of argumentation in a more drastic manner and created Trident NACHOS (Figure 1c). Therein, we increased the cleared hotspot region by creating a larger transversal distance between the pillars that served as spacers and attachment sites for NPs. For placement of the biomolecular assay, a third pillar between the NP attachment pillars was required. This central pillar is designed shorter so that biomolecular assays are placed directly in the equatorial plane between the NPs for optimal FE (Figure 1c).[35]

In this work, we present the Trident DNA origami for biosensing of larger targets with improved kinetics. We optimized the NA design with respect to NP binding and enhancement and drew a comparison of all three NA generations to investigate the impact of less steric constraints in the DNA origami NA hotspot on FE and accessibility. The new Trident NACHOS design thereby aims to improve both FE and accessibility in the plasmonic hotspot, which, ultimately, could be a step forward in democratization of evidence-based health care.[50]

2. Results and Discussion

2.1. DNA Origami Design

In this work, we introduce our next step in the evolution of DNA origami NAs. We specifically sought out the application of this technology for sensing of larger biomolecules on the single-molecule level, making use of the signal enhancement through LSPR. To this end, using a M13mp18-derived scaffold strand we adjusted the design of the previous NACHOS DNA origami to remodel the dimensions of the cleared hotspot region.[42] We expanded the distance between the two outer pillars to 19 nm (dimension in y in Figure 1c and **Figure 2**), leading to a decrease in overall height of the structure to 74 nm and an overall increased width of ≈40.5 nm (Figures S1,S2 and Tables S3,S4, Supporting information).[41] Additionally, the cross-shaped base was rotated by 45° relative to the y–axis compared to the previous Tower NACHOS design (see Figure 1b,c) to facilitate closer binding of both NPs to the central 51 nm high pillar, consisting of eight DNA helices (see colored area in bottom Figure 1c). This creates a designed interparticle distance of 12 nm, which is required for high FE (dimension in x in Figure 2b).[42] To achieve the simultaneous positioning of larger molecules and sufficiently high FE values, a compromise was necessary between structural stability to control NP arrangement and providing a spatially accessible attachment site for molecules in the hotspot region. Simulations using the online tool CanDo were used to estimate the structural rigidity and flexibility of the design (see Experimental Section and Figure S3, Supporting Information).[51] As the new design

includes larger regions cleared from DNA origami, the simulation confirms that features in the Trident, such as the top region of the central pillar are less rigid compared to the more compact Tower NACHOS. Correct folding of the DNA origami structure was confirmed by negative stain transmission electron microscopy (TEM) after purification via ultrafiltration and gel electrophoresis (Figure S4, Supporting Information). Figure 2a and Figure S5, Supporting Information show the formation of the cross-shaped base, designed at 21 nm height, and all three pillars, of which the central one is shorter than the outer two.

To perform bottom-up self-assembly and single-molecule detection on the surface, twelve staple strands on the bottom of the Trident base were replaced with biotinylated oligonucleotides protruding from the structure (Tables S1 and S4, Supporting Information). This allows stable and upright positioning via biotin-NeutrAvidin interaction on a BSA-biotin coated coverslip and is crucial for co-alignment of the NA dipole with incident light.[35] For the purpose of assembling Trident NACHOS on the surface, we extended staple strands in both outlying pillars by a polyadenine sequence (see Figure 2c and Figure S1 and Table S4, Supporting Information). NPs, functionalized with thiolated polythymine ssDNA, are hybridized in zipper geometry to the NP binding strands protruding from the DNA origami at four different heights (46, 51, 53, and 57 nm in z).[36,52] This way, NPs attach in a middle position among the available complementary 20 base pair (bp) binding strands, corresponding to the position with least strain on the formed dsDNA NP binding interactions. By design, this average position of NPs is at the same height as the central pillar, corresponding to the plasmonic hotspot region.[53] A fluorophore, biomolecule, or detection assay of choice is placed in the plasmonic hotspot region between the two NPs via incorporation of the accordingly modified staple in the central pillar. To identify the position of the DNA origami on the surface, the base of the structure was equipped with a localization dye at ≈21 nm height (Figure 2b). The choice of separate excitation wavelengths for the localization and hotspot dye (532 and 639 nm, respectively) enabled colocalization measurements, quantifying the incorporation of molecules in the NA hotspot.[54]

To ensure correct formation of our NAs, we first measured confocal fluorescence scans of immobilized Trident DNA origami before addition of NPs (Figure 2d Reference) and after overnight incubation with 100 nm silver (Ag) NPs (Figure 2d 100 nm Ag NP). We determined the colocalization of red and green spots to 81% ± 5% (Figure S6, Supporting Information), indicating successful labeling of the DNA origami structure with both the localization and hotspot dyes (ATTO542 and ATTO647N, respectively). When observing the sample after incubation with 100 nm AgNPs, confocal scans acquired under the same excitation conditions showed colocalized spots with far higher intensities than in the reference sample, indicating the positioning of the dye (ATTO647N) in the hotspot formed by the NPs. For direct comparison, we recorded fluorescence transients of the NA (violet in Figure 2e) and the reference sample NA (grey in Figure 2e). To ensure the excitation of samples in the linear regime and avoid saturation in the hotspot, transients of NA samples were acquired at 50 nW (200 nW for reference) and normalized to the respective laser power for

**ADVANCED
SCIENCE NEWS**

www.advancedsciencenews.com

**ADVANCED
MATERIALS
INTERFACES**

www.advmatinterfaces.de
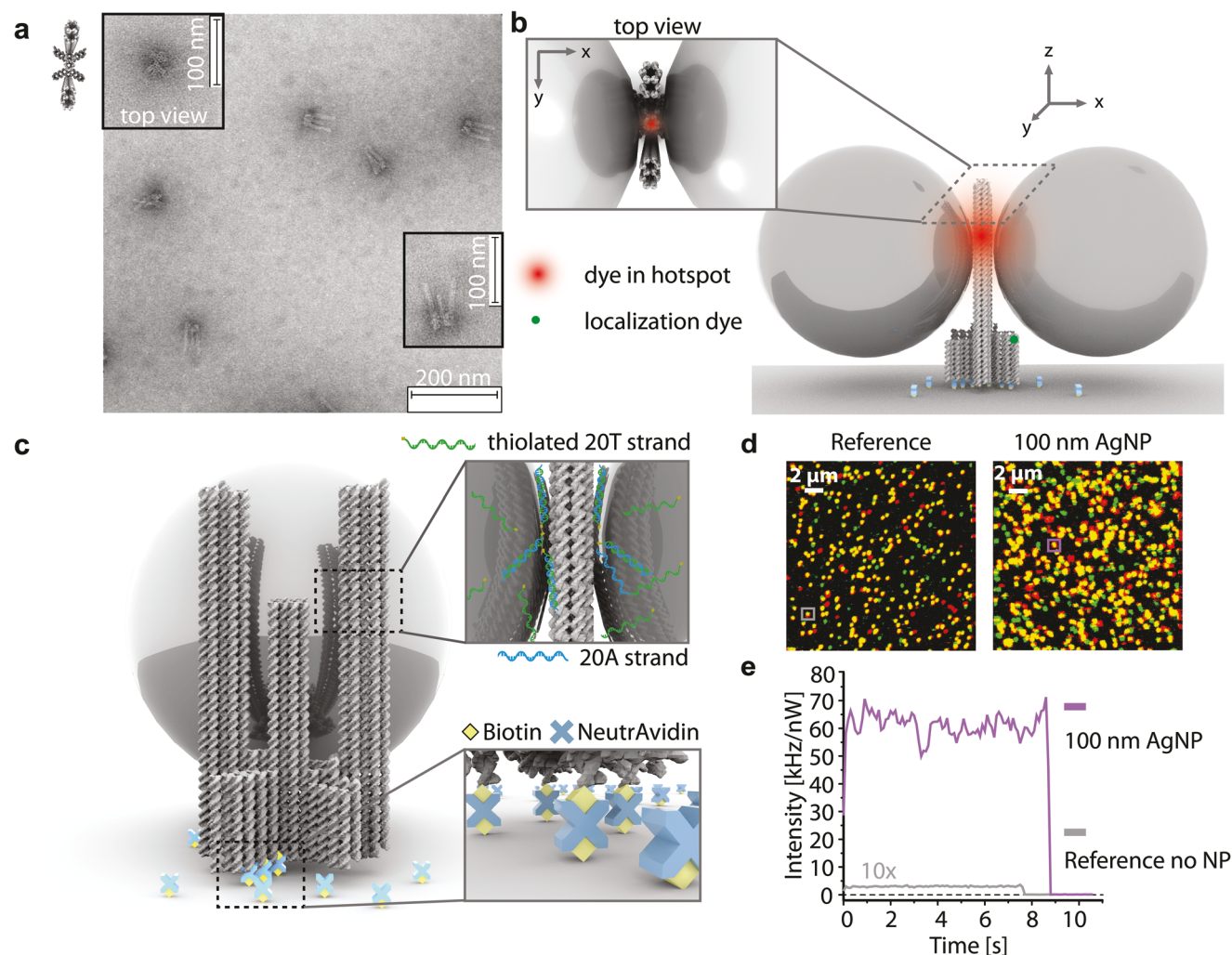
Figure 2. Trident NACHOS design. a) TEM image of the folded and purified structures. b) Schematic representation of the assembled Trident NA including the dye placed in the hotspot (red) and the dye for localization of DNA origami on the surface (green); Inset: top view. c) Strategies for immobilization of the Trident structure on a BSA-biotin-NeutrAvidin coated glass surface and binding NPs. d) Exemplary single-molecule fluorescence scans acquired on a confocal microscope. False-color coded red fluorescence spots obtained from the sample containing 100 nm AgNPs (right) exhibit fluorescence enhancement (FE) for the red fluorophore placed in the hotspot in comparison to the reference (left). Green spots correspond to an ATTO542 molecule for localization of DNA origami. Colocalization of red and green dyes within one construct is indicated by yellow spots. Both images were acquired at laser powers of 2 µW. e) Exemplary fluorescence transients for Trident NA and reference sample. To avoid saturation effects in the hotspot lower excitation powers were chosen for the NP sample (50 nW, reference 200 nW). Intensities were normalized to the laser power, justified as we worked in the linear regime.[43] The intensity of the reference sample without NP was multiplied 10× for visual purposes.

comparison.[43] As seen in both Figure 2d and Figure 2e, the intensity of a single ATTO647N molecule in the hotspot of a 100 nm Ag Trident NA is greatly increased over the dye in the reference sample without NPs.

2.2. Optimizing Conditions for NP Attachment to Trident DNA Origami

After first experiments confirmed the successful incorporation of dye molecules in the hotspot and attachment of NPs, the conditions for formation of the Trident NA were adjusted to reach highest FE values. Stable attachment and

positioning of NPs at the designed distance are required, as the NP-fluorophore distance is one of the parameters determining if the emitter is in the FQ or FE regime. As the proximity to the NP alters the transition rates between electronic states of the fluorophore, the fluorescence lifetime (τ_{fl}) of a dye serves as an indicator for NP attachment. To reach our goal of high FE values, we measured changes in the distribution of τ_{fl} and intensity values of single molecules in samples prepared under different NA formation conditions. FE values were determined after normalization to the respective laser power and by dividing each value for molecules in the NA sample by the mean intensity of all molecules in the reference sample. All spots corresponding to single NAs displayed

2200255 (4 of 11)

in the fluorescence scan images were analyzed and only transients showing single-step bleaching behavior were included. We chose ATTO647N (τ_{fl} of ≈4 ns in reference samples) for the dye in the hotspot, as the long intrinsic lifetime allows to visualize small changes and relatively strong lifetime reductions.

2.2.1. Number of NP Binding Strands on the DNA Origami

As a first step, we determined the influence of different numbers of NP binding strands protruding from the DNA origami structure (**Figure 3**a). We expected an increasing number of accessible binding strands to improve the attachment of NPs and ensure correct positioning of both NPs in the designed distance to each other. The observed trend toward decreased fluorescence lifetimes (Figure 3a, left and Figure S7, Supporting Information)
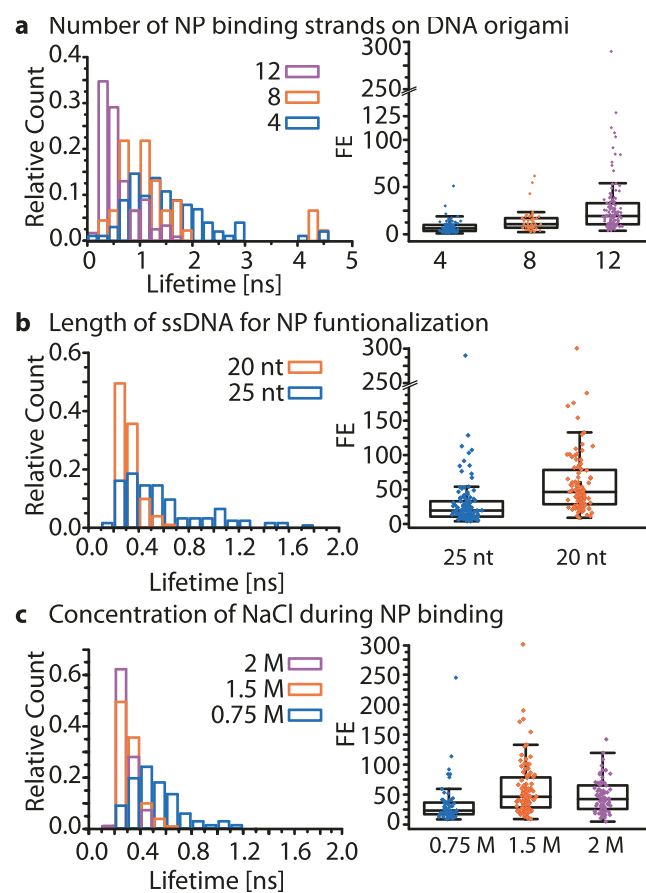
Figure 3. Optimization of τ_{fl} and FE values in the Trident NACHOS structure using an ATTO647N dye molecule in the hotspot. a) Comparison of FE values obtained for different numbers of NP binding strands on the DNA origami. Incubation of 25 nt functionalized NPs in buffer containing 750 mM NaCl. b) Comparing τ_{fl} and FE values obtained for different lengths of strands used for NP functionalization. Comparison was made on Trident with twelve binding strands and buffer containing 750 mM NaCl. c) Effect of NaCl concentration in the NP incubation buffer on τ_{fl} FE values for Trident origami with twelve NP binding strands (20 nt). More than 100 molecules per sample were analyzed. See Figure S7, Supporting Information for scatter plots of fluorescence lifetime versus respective FE values.

and higher FE values of ATTO647N (Figure 3a, middle panel and Figure S7a, Supporting Information) is consistent with this hypothesis. At the same time, the distribution of τ_{fl} (Figure 3a left panel) and τ_{fl}/enhancement plots for the samples containing four and eight NP binding strands (Figure S7a, Supporting Information) shows a substantial fraction of molecules having a lifetime between 1.0 and 3.0 ns. As the accessibility of NP binding strands in the DNA origami could be limited by effects such as molecular threading, we assume that these moderately reduced τ_{fl} values with low FE correspond to a monomer sub-population of NAs in the sample.[54,55] The distribution of data-points for a specifically designed monomer NAs significantly differs from the values we obtained in dimer NACHOS designs. Therefore, we conclude less monomers, but rather a sufficiently high fraction of dimer constructs in NA samples with 8 and 12 NP binding strands (see Figures S2, S7, and S8, Supporting Information and Supplementary Notes). For the Trident DNA origami NA design in particular, these samples demonstrated a clear advantage in forming Trident NAs with high FE values (Figure 3a, right panel and Supplementary Notes). Based on the obtained data, the Trident design containing twelve binding strands was used in the following.

2.2.2. Length of Strands Used for NP Functionalization

Pursuing the goal of optimizing the formation of the Trident NA, we adjusted the length of ssDNA used for functionalization of the 100 nm AgNPs (Figure 3b).[36] Reducing it from 25 to 20 nt on the NP showed an effect on the formation of NAs, as shorter NP binding strands (20 nt, T$_{20}$) led to a more narrowed distribution of τ_{fl} values (concentrated below 1.0 ns, see Figure 3b, left panel) and gave higher FE values than samples with 25 nt NP binding strands (Figure 3b, right panel and Figure S7b, Supporting Information).[36] We hypothesize that shortening the number of interacting nucleotides on NPs that are available for hybridization to DNA origami influences the thermodynamic equilibrium of NP attachment. For shorter interaction lengths the formation of less optimal binding configurations by partial hybridization of strands plays a smaller role.[56] In turn, inter-particle distances that significantly vary from the optimal case, resulting in lower FE values could be reduced when using the interaction of 20 nt for NA formation.[57,58]

2.2.3. Concentration of NaCl during NP Binding

The rate of DNA hybridization is also sensitive to salt (NaCl) concentration. Furthermore, during overnight incubation of the DNA origami with the ssDNA coated NPs the composition of the buffer can influence the stability of the NP functionalization, which also affects potential NP aggregation.[59,60] To this end, we studied the influence of varying NaCl concentrations in the NP incubation buffer (Figure 3c, Figures S7c and S9, Supporting Information, see Experimental Section and Supporting Information for details). While a few molecules at the lowest salt concentration in buffer show τ_{fl} with a maximum of molecules around 0.5 ns (Figure 3c, left panel), highest FE values and reduced τ_{fl} were observed at intermediate (1.5 M) NaCl concentration.

**ADVANCED
SCIENCE NEWS**

www.advancedsciencenews.com

**ADVANCED
MATERIALS
INTERFACES**

www.advmatinterfaces.de

Further increasing the concentration to 2 M NaCl did not improve the values for FE or τ_{fl} (Figure 3c, right panel and Figure S7c, Supporting Information). To sum up, we determined the optimal conditions for Trident NACHOS formation, which include:

I. Using DNA origami structures with 12 NP binding strands.
II. Using NP covered with 20 nt ssDNA.
III. Performing NP incubation at 1.5 M NaCl concentration.

2.3. Comparison of Three DNA Origami Nanoantennas for FE

To compare the efficiency of signal enhancement of the newly designed and optimized Trident structure to that obtained in previous DNA origami NA constructs we evaluated the behavior of a single Alexa Fluor 647 molecule (AF647, $\tau_{fl} \approx 1$ ns) in the hotspot

of a dimer 100 nm Ag NP NA. To reliably detect each fluorophore before photobleaching, a reducing/oxidizing system was used for photostabilization.[61–63] To this end, we prepared separate samples of all three DNA origami structures on the surface and incubated with 100 nm AgNPs (functionalized with T_{20} ssDNA) under the discussed optimal NA formation conditions (Pillar: 6 NP binding strands, 750 mM NaCl; Tower: 12 NP strands, 750 mM NaCl; Trident: 12 NP strands, 1.5 M NaCl). In all three presented structures the central pillar separating both particles of a dimer NA served as the attachment site for molecules in the hotspot and therefore defines the interparticle distance. In this position, the distance of the NPs to each other was estimated to be similar for all three NA structures, as the central pillar consists of a six-helix bundle motif (see Figure 1). Confocal fluorescence scans were first acquired at an excitation power of 2 μW to confirm colocalization of both dyes with the DNA origami. Subsequently, fluorescence transients were recorded (excitation power of 50 nW for NA and 200 nW for reference samples). From the recorded transients, FE values of all DNA origami NA structures were determined by dividing the intensity of each acquired molecule (≥175) by the mean intensity of all molecules (≥190) in the respective reference sample without NPs (grey in left panels of **Figure 4**, Figure S10, Supporting Information). Corresponding fluorescence lifetime values of all molecules were extracted from the acquired fluorescence transients (see Experimental Section). In both NACHOS structures, we measured shorter τ_{fl} and higher mean FE values for a single AF647 molecule placed in the hotspot compared to the Pillar design with a blocked hotspot region (see Figure 4 and **Table 1**). The inherent heterogeneity in all three DNA origami NA samples potentially originates from the multiple factors involved in optimal NA formation, such as functionalization and orientation of NPs, as well as the arrangement of strands in the DNA origami structure itself.[60] Although this is reflected in the broadness of the FE distributions for all three DNA origami designs, the overall trend for the two NACHOS are distributions narrowed to lower τ_{fl} and higher FE values. Comparing the mean FE values for all three designs (grey in right panels of Figure 4) shows similar values for the two NACHOS generations (Tower: 61 ± 46, Trident: 67 ± 58), both higher than for the Pillar design (17 ± 17). The moderate increase in FE might be related to the fact that hybridization of ssDNA-coated NPs to the DNA origami Pillar occurs to the central pillar, creating a slightly larger gap compared to the NACHOS design, where

Figure 4. Comparison of FE and τ_{fl} values obtained for AF647 in the hotspot region of three DNA origami NA structures. Mean FE values were calculated from the arithmetic average and reported with the according standard deviation (SD). a) Pillar NA structure (mean FE: 17 ± 17), b) Tower NACHOS structure (mean FE: 61 ± 46), c) Trident NACHOS structure (mean FE: 67 ± 58). The dashed vertical line corresponds to the obtained mean value of FE. Reference structure corresponds to DNA origami without NPs. Samples were prepared using T_{20} strands for NP functionalization, 6 NP binding strands on the Pillar DNA origami (12 on Tower and Trident), and 750 mM NaCl during NP incubation for Pillar and Tower (1.5 M NaCl for Trident). More than 175 molecules were analyzed for each NA sample, more than 190 for each reference sample.

Table 1. Comparison of designed dimensions and experimentally acquired FE of a single AF647 molecule and sandwich hybridization assay (up to three AF647) in the hotspot of three reported DNA origami structures. Mean FE values were calculated from the arithmetic average and the according SD.[35]

DNA origami design	Pillar	Tower	Trident
Interparticle distance X [nm]	12	12	12
Cleared hotspot width Y [nm]	Blocked by DNA	6.5	19
Overall height Z [nm]	127	84	74
Hotspot position Z [nm]	109	55	51
Cleared hotspot volume [zL]	Blocked by DNA	4.7	7.0
Mean FE for a fixed AF647 dye	17 ± 17	61 ± 46	67 ± 58
Mean FE in diagnostic assay	17 ± 17	69 ± 67	76 ± 57

binding strands protrude from the two outer pillars. We conclude that increasing the size of the plasmonic hotspot region in NACHOS from 6.5 to 19 nm in the transversal direction did not compromise FE (see Table 1) but rather optimized FE by enabling smaller gaps along the longitudinal mode of the NA.

2.4. Comparing the Accessibility of Nanoantenna Hotspots for Binding of 151 nt ssDNA

In our NA approach, capturing large biomolecules in the plasmonic hotspot region is ultimately limited by the diffusion of the molecule into the hotspot of zL volume, which is sterically hindered by DNA origami and NPs. Considering this, it is conceivable that capturing larger molecules might take place on an overall faster timescale for the more open Trident origami design. Additional to limited space in the DNA origami structure, the accessibility of the plasmonic hotspot may also be restricted by the surface of attached NPs (coated with negatively charged DNA). This is particularly relevant for dimer NA constructs containing two large NPs. Geometric approximations for NP attachment result in a theoretical accessible hotspot volume of 4.7 zeptoliters for the dimer Tower NA (Figure S12, Supporting Information). Due to the larger region cleared from
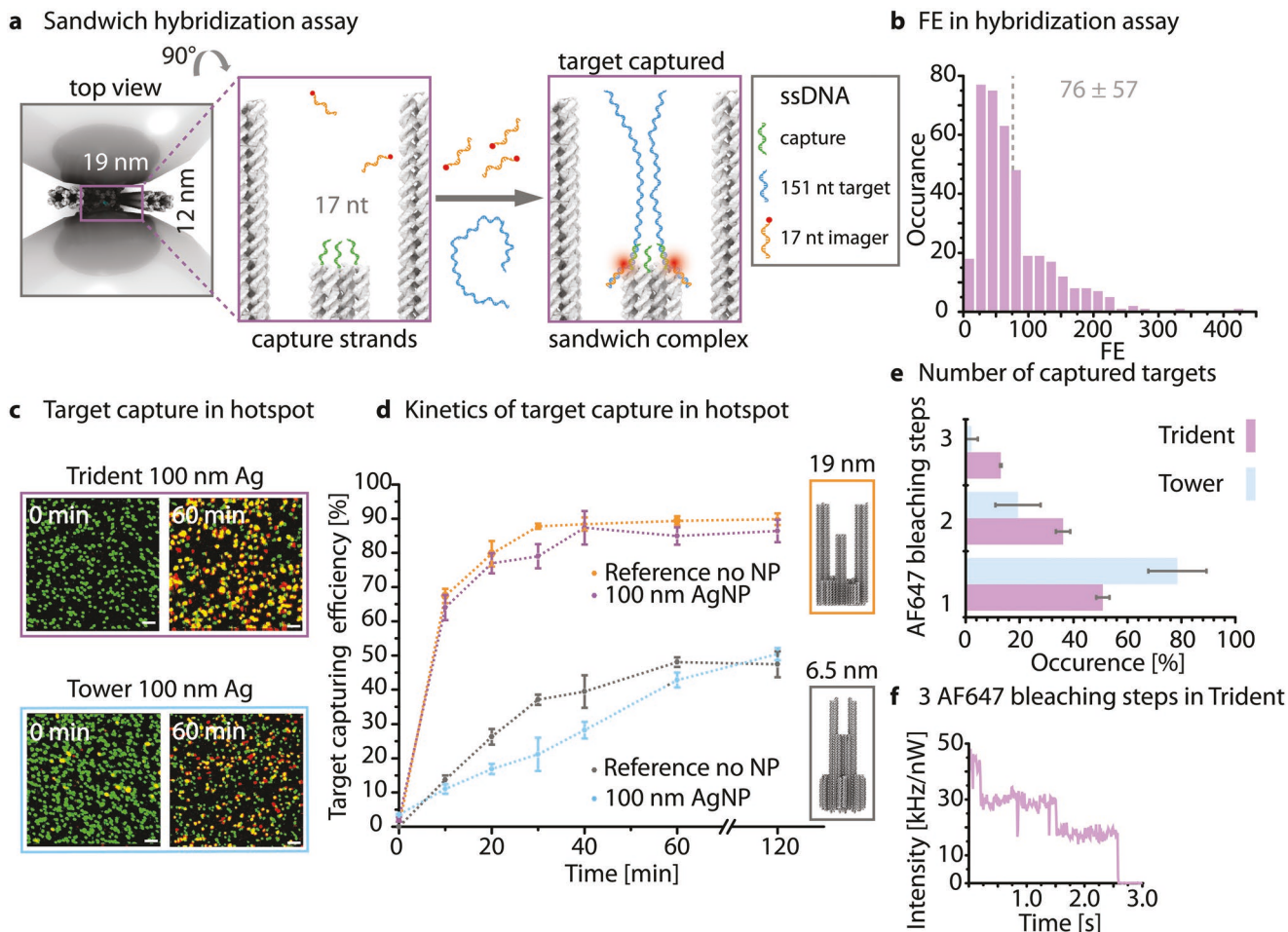
Figure 5. Comparing the accessibility of DNA Origami NA hotspots for the two NACHOS designs. a) Illustration of sandwich hybridization assay for detection of 151 nt target DNA. Addition of both target and 17 nt AF647 labeled imager strands to DNA origami NAs containing three 17 nt capture strands in the hotspots of NACHOS leads to hybridization of the target strand, followed by the binding of the AF647 labeled imager strand in the hotspot and subsequent FE. b) FE values, acquired for AF647 labeled imager strand in Trident NACHOS. 382 single-molecule transients were analyzed. After normalizing to the excitation laser power, each value for molecules in the NA sample was divided by the mean intensity of AF647 molecules in the reference sample without NPs. For multiple bleaching steps, each was considered separately and normalized to the average intensity of a single molecule in the reference sample. c) Confocal fluorescence scans acquired for both NACHOS before and after 60 min incubation with the target/imager solution (4 and 12 nM, respectively). Scale bar corresponds to 2 μm. Exemplary scans for all timepoints in Figure S11, Supporting Information. d) Comparison of kinetics of target capturing obtained for the two structures with different cleared hotspot volumes. Reference Trident without NP (grey); Trident 100 nm AgNP NA (violet); Reference Tower without NP (orange), Tower 100 nm AgNP NA (blue). Dashed lines are included for guiding the eye. (Trident: n ≥ 504 molecules per time point, Tower: n ≥ 791 per time point). e) Quantification of target ssDNA molecules binding in the NA hotspot for the two NACHOS via bleaching step analysis of AF647 after 120 min incubation. Error bars correspond to the standard deviation acquired for three separate measurements. f) Exemplary fluorescence transient for Trident NA with 3 capturing sites exhibiting 3 bleaching steps of AF647. To avoid saturation effects in the hotspot lower excitation powers were chosen for the NP sample (50 nW). Intensities were normalized to the laser power.

ADVANCED
SCIENCE NEWS
www.advancedsciencenews.com

ADVANCED
MATERIALS
INTERFACES
www.advmatinterfaces.de

DNA, the accessible volume of the Trident in and above the designed hotspot at 51 nm height amounts to 7.0 zL and might be accessed more easily due to the larger gaps inside the structure. To prove the increased accessibility of the cleared hotspot region in the new Trident DNA origami NA design and its advantage for diagnostic assays involving larger molecules we carried out a sandwich hybridization assay (**Figure 5**). Therefore, staple strands in the hotspot region were extended by a TTT linker and a 17 nt sequence, creating so-called capture strands which are complementary to part of a 151 nt long, synthetic ssDNA target molecule. We chose a target sequence specific to the OXA-48 gene, that plays an important role in diagnosis of an antibiotic-resistant *Klebsiella pneumonia* infection.[64,65] Binding of the long ssDNA target was visualized by adding a 17 nt AF647 labeled imager strand in solution (Figure 5a and Experimental Section). This strand can hybridize to a 17 nt region within the target ssDNA. Upon capturing both DNA strands inside the NA, the dye is placed in the theoretically optimal position for FE in the plasmonic hotspot. Due to the resulting influence on the fluorophore properties in this position, τ_{fl} and FE of AF647 were used as parameters to confirm positioning of the entire sandwich complex inside the NA hotspot (see Figures S9 and S13, Supporting Information). The overall detection efficiency was quantified via colocalization of the red imager dye with the green ATTO542 labeled DNA origami using confocal microscopy. The amount of red/green colocalized spots (yellow in false-color confocal scans in Figure 5b) was divided by the number of all DNA origamis (green + yellow spots). The resulting values for colocalization of imager dye with the DNA origami NAs are plotted in Figure 5c (all scans in Figure S10, Supporting Information). We performed a comparative study of the Trident NACHOS with the Tower construct to determine the effect of increased dimensions of the region cleared from DNA origami on the accessibility of the hotspot (Trident NA: violet, Tower NA: blue in Figure 5c). To also check for NPs potentially blocking the hotspot region when bound, the two DNA origami structures were prepared both with and without 100 nm AgNPs (Figure 5c Trident: orange, Tower: grey for samples without NP) before incubating with the target/imager solution. Confocal fluorescence scans before incubation (0 min) show only green spots due to the presence of only DNA origami on the surface. In NA samples, apparently colocalized spots appear, for example, due to the effect of NP aggregates scattering (3.5% ± 0.1% in Tower, 2.0% ± 0.7% in Trident), however, the analysis of single-step photobleaching events in fluorescent transients can eliminate this background signal. Already after 10 min of incubation with both target and imager strands (4 and 12 nм, respectively) we measured a notable difference between the amount of the target molecules bound to the capture strand in the hotspot of Tower or Trident DNA origami NAs. 11% ± 1% of ATTO542 labeled Tower DNA origami NAs (blue in Figure 5d) were colocalized with a red AF647 imager in the hotspot. In contrast, after incubating the Trident NA for 10 min with the target/imager mixture, 64% ± 4% of the observed Trident NAs had already bound at least one sandwich complex (violet in Figure 5d, Tower: blue/grey, Trident: violet/orange). Interestingly, our results showed only a small influence of attached NPs on the kinetics of hybridization in the hotspot (Figure 5d), the DNA origami design being a more crucial factor influencing the accessibility of the diagnostic assay. Observing

colocalization as a function of target/imager incubation time indicates overall faster kinetics for binding the sandwich complex in the Trident DNA origami. When comparing the time needed for target capturing to be clearly distinguishable over background (e.g., 30%) this point is reached in less than 10 min for Trident, whereas the Tower NACHOS design requires at least 30 min of incubation. The increased accessibility to the hotspot of the Trident design is further reflected in the overall maximum of visited capture sites in the sample. Trident NACHOS are 87% ± 5% colocalized after 40 min of incubation in comparison to 60 min needed for 43% ± 2% colocalization in Tower NACHOS. Considering that three capturing sites are available to bind the target/imager duplex, single-molecule analysis of colocalized spots gives further insight into how many target molecules were captured in a given design. We acquired fluorescence transients from hundreds of single NAs and used bleaching step analysis to resolve the actual number of AF647 molecules captured by each DNA origami nanostructure both with NPs. As each red spot corresponds to at least one hybridized imager/target complex, the observed number of photobleaching steps of AF647 reports on the number of imager and thus target strands bound in the hotspot (Figure 5d). As for the DNA origami comparison in Figure 4, we used a photostabilizing agent and low excitation powers (50 nW) to ensure the detection of each AF647 molecule before photobleaching. Due to less than 100% labeling efficiency of imager strands, we expected the actual number of bound target molecules to be slightly higher than what was detected in previous NACHOS.[54] The improved accessibility of the larger hotspot is reflected in the increased fraction of NAs capable of capturing multiple target molecules in the Trident DNA origami NA. Three bleaching steps, and thereby occupation of all available capturing sites by a sandwich complex were observed in 13% of the Trident NA origami in the sample (4% in Tower). The fraction of NAs binding two target molecules also increased to 36% in the Trident DNA origami NA over 19% in the Tower design. Accordingly, the ratio of spots in the sample that exhibit only one photobleaching step of the dye in the hotspot decreased from 79% for Tower to 51% in Trident NA samples. While the increased dimensions of the Trident NACHOS hotspot clearly improved its accessibility, the attained FE within this NA structure was not compromised (Figures S12, S14, and S15, Supporting Information). As shown in Table 1 the obtained FE values for the diagnostic assay placed in the Trident structure are distributed around a maximum of 76 ± 57 and therefore are even slightly higher than the FE values we acquired for a fixed AF647 dye in the Trident DNA origami NA hotspot.

3. Conclusion

We presented a novel Trident DNA origami design for NACHOS to detect larger targets, such as a 151 nt long ssDNA. The Trident DNA origami architecture was optimized for NA formation, by reducing the length and increasing the number of NP binding strands, as well as optimizing the NP binding conditions.

We then compared the Trident NACHOS to previous designs and found that FE in the Trident NACHOS was similar to or better than in previous NA realizations (see summary in

**ADVANCED
SCIENCE NEWS**

www.advancedsciencenews.com

**ADVANCED
MATERIALS
INTERFACES**

www.advmatinterfaces.de

Table 1, Figure S15, Supporting Information). The advantage of the newly presented DNA origami Trident design lies in the increased accessibility of the plasmonic hotspot region. We expanded the cleared space between the two pillars for NP attachment to 19 nm, while keeping the interparticle distance equal to the previous designs. This enabled not only the detection of a 151 nt ssDNA target molecule with improved binding yield, but also accelerated binding kinetics. This was demonstrated by, for example, 30% of the DNA origami binding at least one target/imager construct in under 10 min, corresponding an approximately threefold increase in speed compared to the Tower NACHOS. Further, the plateau of target molecule binding, representing the maximum hotspot accessibility was higher in Trident NACHOS and reached faster than in the Tower design. Incorporating microfluidic methods to increase mass transport should further improve the assay speed and bring it into a relevant range of sensitivity for many applications.[66–68] While the DNA origami design played a key role, attachment of NPs interestingly only had a minimal influence on hotspot accessibility and binding kinetics.

The achieved duality of high FE values and improved accessibility of the hotspot region expands the applicability of our technology for single-molecule-based plasmonic biosensing, thereby making it possible to carry out an assay with cost-effective and mobile optical equipment.[42] The presented binding of multiple target DNA molecules in our Trident NA hotspot suggests the feasibility of multiplexed detection within one NA. In this manner, the capturing of several target DNA molecules with varying sequences inside one Trident NACHOS construct is conceivable. In turn, each sequence then could be visualized using spectrally separate imager strands. Furthermore, the large clearing in the hotspot could also facilitate placement of active proteins in the plasmonic hotspots (e.g., polymerases), thereby expanding the application of DNA origami NAs to different avenues, such as nanopore plasmonics, DNA sequencing, or detailed studies of transition paths in conformational dynamics of protein folding inside the plasmonic hotspot.[68–77]

4. Experimental Section

DNA Origami Design, Folding, and Purification: DNA origami structures were designed and adapted in CaDNAno version 2.3.0 (staple layout in Figure S1 and Table S4, Supporting Information).[4] Simulations to estimate structural rigidity and flexibility were performed using the online tool CanDo (Figure S3 and Table S1, Supporting Information).[6,51] The DNA origami structures were prepared by performing previously published protocols in adaption of Wagenbauer et al.[39] For preparation of the Trident DNA origami, 25 µL of 100 nm in-house produced p8064 scaffold strand solution was combined with tenfold excess of staple strands (Integrated DNA Technologies Europe GmbH, Germany; Eurofins Genomics GmbH, Germany and biomers.net GmbH, Germany). To simplify the process, mastermix solutions of modified and unmodified staple strands were pooled from their 100 µm concentration. 18 µL of unmodified staples, together with 2 µL modified strands were added to the scaffold and filled up with 2.5 µL 10 × FoB20 (containing Tris, EDTA, MgCl2, and NaCl, see Table S2, Supporting Information for recipe). Table S3, Supporting Information shows adapted recipes for Tower and Pillar DNA origami. Heating to 95 °C and cooling down to 25 °C were performed according to the annealing ramp shown in Table S5, Supporting Information. Excess staple strands were removed by purifying with Amicon filtering through a 100 kDa MWCO membrane

(Merck KGaA, Germany). The mixture was purified by centrifugation at 20 °C and 10 000 × g for 5 min after washing with 1 × FoB5; the procedure was performed five times. The Amicon filter was then flipped and placed in a new Amicon tube, centrifuging at 1000 rpm at 20 °C for 1 min to extract the purified DNA origami. The presence of DNA origami in the solution was confirmed and quantified via UV-vis spectroscopy (NanoDrop, Fischer Scientific, USA). Determined yields from synthesis using 100 nm scaffold strand were commonly in the range of 72 ± 18 nm.

TEM: TEM grids (Formvar/carbon, 400 mesh, Cu, TedPella, Inc. USA) were cleaned in Ar-plasma and incubated for 60 s with the DNA origami sample (5 µL, ≈2 to 10 nm). 2% uranyl formeate solution (5 µL) was used to wash the grids and incubate 4 s for staining. Imaging was performed on a JEM-1100 microscope (JEOL GmbH, Japan) with acceleration voltage of 80 kV.

Silver NP Functionalization: Functionalization of plasmonic NPs with ssDNA was performed using a modification of a published protocol.[39] During the entire preparation procedure 2 mL of the NP solution (1 mg mL^{-1} 100 nm Ag, BioPure Silver Nanospheres (in 2 mm Citrate), nanoComposix, USA) were continuously stirred at 550 rpm at 40 °C. In the following, 20 µL of polysorbate 20 (10%, Sigma Aldrich, USA), as well as 20 µL potassium phosphate buffer (1 m solutions of mono- and dibasic potassium phosphate in a 4:5 mixture, Sigma Aldrich, USA) and 10 µL of a 2 nm thiol-modified single stranded DNA solution (5″-thiol-25T-3″ or 5″-thiol-20T-3,″ Ella Biotech GmbH) were added successively. The mixture was then stirred at 40 °C for 1 h. To reach a final concentration 750 mm of NaCl in PBS3300 buffer (see Table S2, Supporting Information) a salting procedure was performed by gradually adding portions of the buffer over a period of 45 min (see Table S6, Supporting Information). The solution was then diluted 1:1 with PBS 10 buffer (1 × PBS, 10 mm NaCl, 2.11 mm P8709, 89 mm P8584 (Sigma Aldrich, USA), 0.01% polysorbate 20, and 1 mm EDTA (Thermo Fisher Scientific, USA)). Excess of thiolated ssDNA was removed by centrifuging the solution for 10 min at 2800 × g and 20 °C. After centrifugation, the supernatant was discarded and the pellet containing the concentrated particles was again dissolved in PBS 10 buffer. This washing step was repeated four times. The silver NPs were then diluted in 1 × TE containing 750 mm, 1.5 m, or 2 m of NaCl to reach an approximate value of 0.1 for the extinction maximum on the UV-Vis spectrometer (Nanodrop 2000, Thermo Fisher, USA).

Nanoantenna Preparation: To prepare the surface for immobilization of DNA origami microscope coverslips (24 mm × 60 mm and 170 µm thickness) were UV-Ozone cleaned (PSD-UV4, Novascan Technologies, USA). SecureSeal Hybridization Chambers (2.6 mm depth, Grace Bio-Labs, USA) were glued on the clean coverslips and laid on a heating plate (1 min at 80 °C) to ensure sufficient sealing. The obtained chambers were washed three times with 1 × PBS buffer. Bovine serum albumin (BSA)-biotin (1 mg mL^{-1}, Sigma Aldrich, USA) was used to passivate the surface and incubated for 30 min. After washing the chambers 3 × with 1 × PBS, NeutrAvidin 0.25 mg mL^{-1} (Sigma Aldrich, USA) was added and incubated for 30 min. Afterward, three washing steps with 1 × PBS were performed. The purified DNA origami solution was diluted in TE buffer containing 750 mm NaCl (TE750) to prepare a solution with concentration in a range between 250 and 400 pm. After 5 min of incubating with the diluted DNA origami solution, three washing steps were performed with TE750 buffer. Afterward, appropriate surface density for single-molecule measurements was confirmed on the microscope (see "Confocal Microscopy, Data, and Statistical Analysis" in Experimental Section). AgNPs solution was added and incubated in the TE buffer (see Table S2, Supporting Information) containing 750 mm, 1.5 m, or 2 m of NaCl. After overnight incubation, samples were washed three times with the same buffer. Afterward, the surface was stored in TE750 to avoid drying and degradation of the samples.

Sandwich Hybridization Assay: DNA origami structures were folded containing three capture strands (see sequences in Table S4, Supporting Information) for the 151 nt DNA target, specific to the OXA-48 gene carrying the antibiotic resistance.[64,65] Prepared NA samples were incubated with 4 nm target DNA (Table S4, Supporting Information) and 12 nm AF647 labeled imager strand (17 nt, see Table S4, Supporting

Information) in 1 × TE containing 2 M NaCl and 0.01% polysorbate 20 (Sigma Aldrich, USA) for the denoted amount of time. After incubation, samples were washed three times with the incubation buffer and stored in TE750 for imaging.

Confocal Microscopy, Data, and Statistical Analysis: To detect the fluorescence of single molecules a custom-build setup based on an Olympus IX-83 inverted microscope (Olympus Corporation, Japan) with a 78 MHz pulsed supercontinuum white-light laser (SuperK Extreme, NKT Photonics A/S, Denmark) was used. Wavelength selection between 532 and 639 nm was achieved with an acousto-optically tunable filter (AOTF, SuperK Dual AOTF, NKT Photonics, Denmark) and a digital controller (AODS 20160 8R, Crystal Technology, Inc., USA) via computer software (AODS 20160 Control Panel, Crystal Technology, Inc. USA). A second AOTF (AA.AOTF. ns: TN, AA-Opto-Electronic, France) was used to alternate between the two wavelengths if required. The second AOTF, controlled via LabVIEW software, was further used to set laser intensity and spectrally clean the laser beam. A neutral density filter (ndF, OD 0-2, Thorlabs, Germany) was used to manually regulate the laser intensity followed by a linear polarizer (LPVISE100-A, Thorlabs, Germany) and lambda quarter plate (AQWP05M-600, Thorlabs, Germany) for circular polarized excitation. The height difference between excitation path and microscope body was overcome in the setup by coupling the laser into a polarization maintaining fiber (PM-Faser, P1-488PM-FC-2, Thorlabs, Germany). The laser was focused onto the sample with an oil-immersion objective (UPlanSApo100×, NA = 1.4, WD = 0.12 mm, Olympus Corporation, Japan). Positioning of the sample was performed with a piezo stage (P-517.3CL, E-501.00, Physik Instrumente GmbH & Co. KG, Germany). Excitation light was separated from the emitted light through the dichroic beam splitter and then focused on a 50 μm pinhole (Linos AG, Germany). The emission channels for red and green were spectrally filtered (red: RazorEdge 647, Semrock Inc., USA and green: Brightline HC582/75, Semrock Inc, USA). The light was detected by a Single-Photon Avalanche Diode (SPCM, AQR 14, PerkinElmer Inc., USA) and registered by a TCSPC system (HydraHarp 400, PicoQuant GmbH, Germany). Settings for scans were 2 μW, powers of 50 nW were used to record transients of samples with NPs, 200 nW for samples without NPs. A custom-made LabVIEW software (National Instruments, USA) was used to process the acquired data. Background correction was performed for each transient. Fluorescence lifetime decays were extracted and monoexponentially fitted for the shortest lifetime component. Datapoints presented in Figure 4 were further deconvolved from the instrument response function using FluoFit (PicoQuant GmbH, Germany). FE values were determined by dividing intensity values of every NA sample by the mean intensity measured in the reference sample, normalized by the set laser power. The extracted data were analyzed in OriginPro2019. Samples were prepared according to the protocol described above. Samples containing AF647 were imaged in a reducing and oxidizing buffer system for enzymatic oxygen removal (ROXS, see Table S2, Supporting Information).

Supporting Information

Supporting Information is available from the Wiley Online Library or from the author.

Acknowledgements

Conflict of Interest

The authors declare no conflict of interest.

Data Availability Statement

The data that support the findings of this study are available from the corresponding author upon reasonable request.

Keywords

[1] N. C. Seeman, *J. Theor. Biol.* **1982**, *99*, 237.
[2] N. C. Seeman, A. M. Belcher, *Proc. Natl. Acad. Sci. USA* **2002**, *99*, 6451.
[3] P. W. K. Rothemund, *Nature* **2006**, *440*, 297.
[4] S. M. Douglas, A. H. Marblestone, S. Teerapittayanon, A. Vazquez, G. M. Church, W. M. Shih, *Nucleic Acids Res.* **2009**, *37*, 5001.
[5] S. M. Douglas, H. Dietz, T. Liedl, B. Hogberg, F. Graf, W. M. Shih, *Nature* **2009**, *459*, 414.
[6] C. E. Castro, F. Kilchherr, D. N. Kim, E. L. Shiao, T. Wauer, P. Wortmann, M. Bathe, H. Dietz, *Nat. Methods* **2011**, *8*, 221.
[7] D. R. Walt, *Anal. Chem.* **2013**, *85*, 1258.
[8] M. Bauch, K. Toma, M. Toma, Q. Zhang, J. Dostalek, *Plasmonics* **2014**, *9*, 781.
[9] E. D. Fabrizio, S. Schlücker, J. Wenger, R. Regmi, H. Rigneault, G. Calafiore, M. West, S. Cabrini, M. Fleischer, N. F. van Hulst, M. F. Garcia-Parajo, A. Pucci, D. Cojoc, C. A. E. Hauser, M. Ni, *J. Opt.* **2016**, *18*, 063003.
[10] A. B. Taylor, P. Zijlstra, *ACS Sens.* **2017**, *2*, 1103.
[11] M. Madsen, K. V. Gothelf, *Chem. Rev.* **2019**, *119*, 6384.
[12] S. Wang, Z. Zhou, N. Ma, S. Yang, K. Li, C. Teng, Y. Ke, Y. Tian, *Sensors* **2020**, *20*, 6899.

**ADVANCED
SCIENCE NEWS**

www.advancedsciencenews.com

**ADVANCED
MATERIALS
INTERFACES**

www.advmatinterfaces.de

[13] S. Dey, C. Fan, K. V. Gothelf, J. Li, C. Lin, L. Liu, N. Liu, M. A. D. Nijenhuis, B. Saccà, F. C. Simmel, H. Yan, P. Zhan, *Nat. Rev. Methods Primers* **2021**, *1*, 13.

[14] F. Hong, F. Zhang, Y. Liu, H. Yan, *Chem. Rev.* **2017**, *117*, 12584.

[15] P. Kuhler, E. M. Roller, R. Schreiber, T. Liedl, T. Lohmuller, J. Feldmann, *Nano Lett.* **2014**, *14*, 2914.

[16] V. Giannini, A. I. Fernandez-Dominguez, S. C. Heck, S. A. Maier, *Chem. Rev.* **2011**, *111*, 3888.

[17] J. M. Kim, C. Lee, Y. Lee, J. Lee, S. J. Park, S. Park, J. M. Nam, *Adv. Mater.* **2021**, *33*, 2006966.

[18] Y. Fu, J. R. Lakowicz, *Laser Photonics Rev.* **2009**, *3*, 221.

[19] P. Anger, P. Bharadwaj, L. Novotny, *Phys. Rev. Lett.* **2006**, *96*, 113002.

[20] R. Carminati, J. J. Greffet, C. Henkel, J. M. Vigoureux, *Opt. Commun.* **2006**, *261*, 368.

[21] G. P. Acuna, M. Bucher, I. H. Stein, C. Steinhauer, A. Kuzyk, P. Holzmeister, R. Schreiber, A. Moroz, F. D. Stefani, T. Liedl, F. C. Simmel, P. Tinnefeld, *ACS Nano* **2012**, *6*, 3189.

[22] R. Chikkaraddy, V. A. Turek, N. Kongsuwan, F. Benz, C. Carnegie, T. van de Goor, B. de Nijs, A. Demetriadou, O. Hess, U. F. Keyser, J. J. Baumberg, *Nano Lett.* **2018**, *18*, 405.

[23] V. V. Thacker, L. O. Herrmann, D. O. Sigle, T. Zhang, T. Liedl, J. J. Baumberg, U. F. Keyser, *Nat. Commun.* **2014**, *5*, 3448.

[24] J. Prinz, B. Schreiber, L. Olejko, J. Oertel, J. Rackwitz, A. Keller, I. Bald, *J. Phys. Chem. Lett.* **2013**, *4*, 4140.

[25] M. Moskovits, *J. Raman Spectrosc.* **2005**, *36*, 485.

[26] K. A. Willets, R. P. Van Duyne, *Annu. Rev. Phys. Chem.* **2007**, *58*, 267.

[27] K. Tapio, A. Mostafa, Y. Kanehira, A. Suma, A. Dutta, I. Bald, *ACS Nano* **2021**, *15*, 7065.

[28] M. Dass, F. N. Gur, K. Kolataj, M. J. Urban, T. Liedl, *J. Phys. Chem. C* **2021**, *125*, 5969.

[29] C. Vietz, I. Kaminska, M. Sanz Paz, P. Tinnefeld, G. P. Acuna, *ACS Nano* **2017**, *11*, 4969.

[30] P. Bharadwaj, L. Novotny, *Opt. Express* **2007**, *15*, 14266.

[31] P. Holzmeister, E. Pibiri, J. J. Schmied, T. Sen, G. P. Acuna, P. Tinnefeld, *Nat. Commun.* **2014**, *5*, 5356.

[32] H. Chew, *Phys. Rev. A* **1988**, *38*, 3410.

[33] A. Kinkhabwala, Z. Yu, S. Fan, Y. Avlasevich, K. Müllen, W. E. Moerner, *Nat. Photonics* **2009**, *3*, 654.

[34] J. Seelig, K. Leslie, A. Renn, S. Kühn, V. Jacobsen, M. Van De Corput, C. Wyman, V. Sandoghdar, *Nano Lett.* **2007**, *7*, 685.

[35] V. Glembockyte, L. Grabenhorst, K. Trofymchuk, P. Tinnefeld, *Acc. Chem. Res.* **2021**, *54*, 3338.

[36] C. Vietz, B. Lalkens, G. P. Acuna, P. Tinnefeld, *New J. Phys.* **2016**, *18*, 045012.

[37] G. P. Acuna, F. M. Möller, P. Holzmeister, S. Beater, B. Lalkens, P. Tinnefeld, *Science* **2012**, *338*, 506.

[38] C. A. Mirkin, R. L. Letsinger, R. C. Mucic, J. J. Storhoff, *Nature* **1996**, *382*, 607.

[39] S. E. Ochmann, C. Vietz, K. Trofymchuk, G. P. Acuna, B. Lalkens, P. Tinnefeld, *Anal. Chem.* **2017**, *89*, 13000.

[40] C. Vietz, B. Lalkens, G. P. Acuna, P. Tinnefeld, *Nano Lett.* **2017**, *17*, 6496.

[41] J. J. Schmied, C. Forthmann, E. Pibiri, B. Lalkens, P. Nickels, T. Liedl, P. Tinnefeld, *Nano Lett.* **2013**, *13*, 781.

[42] K. Trofymchuk, V. Glembockyte, L. Grabenhorst, F. Steiner, C. Vietz, C. Close, M. Pfeiffer, L. Richter, M. L. Schutte, F. Selbach, R. Yaadav, J. Zahringer, Q. Wei, A. Ozcan, B. Lalkens, G. P. Acuna, P. Tinnefeld, *Nat. Commun.* **2021**, *12*, 950.

[43] L. Grabenhorst, K. Trofymchuk, F. Steiner, V. Glembockyte, P. Tinnefeld, *Methods Appl. Fluoresc.* **2020**, *8*, 024003.

[44] M. Pfeiffer, K. Trofymchuk, S. Ranallo, F. Ricci, F. Steiner, F. Cole, V. Glembockyte, P. Tinnefeld, *iScience* **2021**, *24*, 103072.

[45] K. Huebner, H. Joshi, A. Aksimentiev, F. D. Stefani, P. Tinnefeld, G. P. Acuna, *ACS Nano* **2021**, *15*, 5109.

[46] V. Kaur, S. Tanwar, G. Kaur, T. Sen, *ChemPhysChem* **2021**, *22*, 160.

[47] P. Zhan, T. Wen, Z. G. Wang, Y. He, J. Shi, T. Wang, X. Liu, G. Lu, B. Ding, *Angew. Chem., Int. Ed.* **2018**, *57*, 2846.

[48] T. Zhang, N. Gao, S. Li, M. J. Lang, Q. H. Xu, *J. Phys. Chem. Lett.* **2015**, *6*, 2043.

[49] D. Wang, S. L. Capehart, S. Pal, M. Liu, L. Zhang, P. J. Schuck, Y. Liu, H. Yan, M. B. Francis, J. J. De Yoreo, *ACS Nano* **2014**, *8*, 7896.

[50] I. Hernandez-Neuta, F. Neumann, J. Brightmeyer, T. Ba Tis, N. Madaboosi, Q. Wei, A. Ozcan, M. Nilsson, *J. Intern. Med.* **2019**, *285*, 19.

[51] D. - N. Kim, F. Kilchherr, H. Dietz, M. Bathe, *Nucleic Acids Res.* **2012**, *40*, 2862.

[52] S. J. Hurst, A. K. R. Lytton-Jean, C. A. Mirkin, *Anal. Chem.* **2006**, *78*, 8313.

[53] X. Wei, J. Nangreave, Y. Liu, *Acc. Chem. Res.* **2014**, *47*, 1861.

[54] M. T. Strauss, F. Schueder, D. Haas, P. C. Nickels, R. Jungmann, *Nat. Commun.* **2018**, *9*, 1600.

[55] N. Wu, D. M. Czajkowsky, J. Zhang, J. Qu, M. Ye, D. Zeng, X. Zhou, J. Hu, Z. Shao, B. Li, C. Fan, *J. Am. Chem. Soc.* **2013**, *135*, 12172.

[56] E. Sambriski, D. Schwartz, J. De Pablo, *Proc. Natl. Acad. Sci. USA* **2009**, *106*, 18125.

[57] H. Ramezani, H. Dietz, *Nat. Rev. Genet.* **2020**, *21*, 5.

[58] P. C. Whitford, J. N. Onuchic, *Curr. Opin. Struct. Biol.* **2015**, *30*, 57.

[59] M. Horacek, R. E. Armstrong, P. Zijlstra, *Langmuir* **2018**, *34*, 131.

[60] M. Horacek, D. J. Engels, P. Zijlstra, *Nanoscale* **2020**, *12*, 4128.

[61] T. Cordes, J. Vogelsang, P. Tinnefeld, *J. Am. Chem. Soc.* **2009**, *131*, 5018.

[62] T. Ha, P. Tinnefeld, *Annu. Rev. Phys. Chem.* **2012**, *63*, 595.

[63] J. Vogelsang, R. Kasper, C. Steinhauer, B. Person, M. Heilemann, M. Sauer, P. Tinnefeld, *Angew. Chem., Int. Ed.* **2008**, *47*, 5465.

[64] L. Poirel, C. Héritier, V. Tolün, P. Nordmann, *Antimicrob. Agents Chemother.* **2004**, *48*, 15.

[65] J. Hrabák, E. Chudáčkova, C. C. Papagiannitsis, *Clin. Microbiol. Infect.* **2014**, *20*, 839.

[66] P. Pattanayak, S. K. Singh, M. Gulati, S. Vishwas, B. Kapoor, D. K. Chellappan, K. Anand, G. Gupta, N. K. Jha, P. K. Gupta, P. Prasher, K. Dua, H. Dureja, D. Kumar, V. Kumar, *Microfluid. Nanofluid.* **2021**, *25*, 99.

[67] X. Weng, H. Jiang, D. Li, *Microfluid. Nanofluid.* **2011**, *11*, 367.

[68] H. S. Chung, K. McHale, J. M. Louis, W. A. Eaton, *Science* **2012**, *335*, 981.

[69] J. Hahn, L. Y. T. Chou, R. S. Sorensen, R. M. Guerra, W. M. Shih, *ACS Nano* **2020**, *14*, 1550.

[70] J. Eid, A. Fehr, J. Gray, K. Luong, J. Lyle, G. Otto, P. Peluso, D. Rank, P. Baybayan, B. Bettman, A. Bibillo, K. Bjornson, B. Chaudhuri, F. Christians, R. Cicero, S. Clark, R. Dalal, A. deWinter, J. Dixon, M. Foquet, A. Gaertner, P. Hardenbol, C. Heiner, K. Hester, D. Holden, G. Kearns, X. Kong, R. Kuse, Y. Lacroix, S. Lin, et al., *Science* **2009**, *323*, 133.

[71] V. Jadhav, D. P. Hoogerheide, J. Korlach, M. Wanunu, *Nano Lett.* **2019**, *19*, 921.

[72] T. Gilboa, C. Torfstein, M. Juhasz, A. Grunwald, Y. Ebenstein, E. Weinhold, A. Meller, *ACS Nano* **2016**, *10*, 8861.

[73] J. D. Spitzberg, A. Zrehen, X. F. van Kooten, A. Meller, *Adv. Mater.* **2019**, *31*, e1900422.

[74] R. Wang, T. Gilboa, J. Song, D. Huttner, M. W. Grinstaff, A. Meller, *ACS Nano* **2018**, *12*, 11648.

[75] M. Belkin, S. - H. Chao, M. P. Jonsson, C. Dekker, A. Aksimentiev, *ACS Nano* **2015**, *9*, 10598.

[76] F. Nicoli, D. Verschueren, M. Klein, C. Dekker, M. P. Jonsson, *Nano Lett.* **2014**, *14*, 6917.

[77] D. Garoli, H. Yamazaki, N. Maccaferri, M. Wanunu, *Nano Lett.* **2019**, *19*, 7553.